Inorganic Chemistry

pubs.acs.org/IC

Article

Solvothermal and Ultrasonic Preparation of Two Unique Cluster-Based Lu and Y Coordination Materials: Metal–Organic Framework-Based Ratiometric Fluorescent Biosensor for an Ornidazole and Ronidazole and Sensing Platform for a Biomarker of Amoeba Liver Abscess

Xing Ze Wang, Xin Yu Mao, Zi Qing Zhang, Rui Guo, Yi Yun Zhang, Na Jia Zhu, Kuo Wang, Ping Ping Sun, Jian Zhong Huo, Xin Rui Wang,* and Bin Ding*

Cite This: https://dx.doi.org/10.1021/acs.inorgchem.9b03272

ABSTRACT: Through powerful solvothermal and facile ultrasonic synthetic strategies, two unique cluster-based lanthanide Lu and Y nanoporous metal organic frameworks (MOFs) have been successfully prepared, namely, $\{[Lu_2(L)_2]\cdot 2DMF\cdot H_2O\}_n$ (**Lu-MOF**) and $[Y(L)(DMF)_{0.75}]_n$ (**Y-MOF**) (H_3L = terphenyl-3,4′′,5-tricarboxylic acid). In addition, both the morphologies and nanosizes of **Lu-MOF** and **Y-MOF** materials also have been deliberately tuned by adjustable ultrasonic conditions including irradiation time (40, 60, and 80 min) and power (70 w, 100 w). Currently, it is noted that the abuse of antibiotics such as ornidazole and ronidazole leads to great damage to human health, and therefore the development of highly effective and facile detection methods for ornidazole and ronidazole is quite important. Herein, to improve the fluorescent sensing sensitivity of antibiotics, Eu^{3+} and Tb^{3+} have been introduced into **Lu-MOF** (under a solvothermal preparation method) to fabricate a dual-emission hybrid material **Eu^{3+}/Tb^{3+}@Lu-MOF** through a postsynthesis strategy, which can be successfully applied as a self-calibrated ratiometric fluorescent sensor for ornidazole and ronidazole with high selectivity and sensitivity (the K_{sv} value for ornidazole is 1.0854×10^6 [M^{-1}], and the K_{sv} value for ronidazole is 1.0595×10^7 [M^{-1}]) and low detection limit values (2.85 nM for ornidazole and 26.7 nM for ronidazole). On the other hand, amoeba liver abscess (ALA) will easily lead to irregular fever, night sweats, and other tortured symptoms; C-reactive protein autoantibody (CRP Ab) is the important biomarker for the detection of ALA. Given this, **Y-MOF** (under the solvothermal preparation method) also has been successfully designed to combine FAM-labeled NH-ssDNA to construct the scarcely reported excellent hybrid FAM-labeled NH-ssDNA/**Y-MOF** sensing platform for the highly effective discrimination of CRP Ab with excellent sensitivity and selectivity in real samples such as human serum solution.

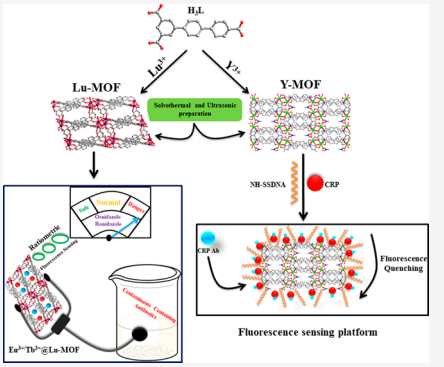

1. INTRODUCTION

Recently, lanthanide metal–organic frameworks (LMOFs)[1−4] have attracted many scientists' attention because these functional materials possess high and stable luminescent efficiency due to very weak ligand-field effects. In addition, these rare-earth centers possess high coordination numbers and variable coordination geometries,[5,6] which can result in the construction of flexible structures and affect the interface interaction with target molecules.[7−9] On the other hand, selecting suitable ligands to fabricate lanthanide MOFs based sensors[10,11] to detect target molecules also needs to be considered. Indispensable considerations for these lanthanide MOFs based sensors should be given including the strong conjugated structure, specific functional groups, and highly stable framework structures in the detection process.[12] Furthermore, it should be noted that work on the preparation and application of lanthanide Lu-based and Y-based MOFs is still scarcely reported.[13−15] However, Lu-based MOF and Y-based MOF show great potential applications. For example, previously Rybak et al. have reported the interesting polymorphism of an isotypic series of heavy lanthanides Gd–Lu based MOFs, which can be tuned from open to dense frameworks of varying dimensionality.[16]

Although these lanthanide MOFs have highly stable luminescent efficiency, single chromophores still may be easily influenced by other external interference factors such as optical occlusion, atmosphere, excitation power fluctuation, and pressure. However, these ratiometric fluorescent sensors[17−19]

Received: November 7, 2019

Scheme 1. Illustration of Self-Assembled Eu^{3+}/Tb^{3+}@Lu-MOF

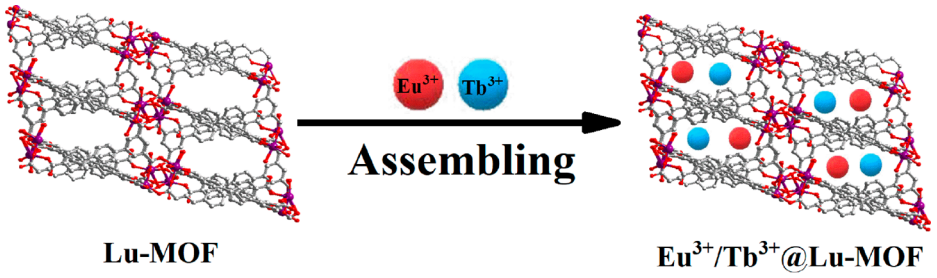

can be constructed based on the emission intensity ratio of two independent fluorescence signal bands, which can circumvent many external complications, and thus these ratiometric fluorescent sensors are gathering more attention.[20] For example, Qian's group[21] designed and prepared luminescent lanthanide metal−organic frameworks (LnMOFs) applied in cryogenic temperature sensing. By utilizing the lanthanides codoping strategy, an unique Tb^{3+}/Eu^{3+} mixed LnMOF system $Tb_{1-x}Eu_xFTPTC$ (x = 0.05, 0.1, 0.2) has been developed that features excellent linear responses to temperature with a high relative sensitivity in the cryogenic range of 25−125 K. Designing and applying the ratiometric fluorescent sensors will benefit improved sensitivity in the detection systems.

Up to now, there are many synthetic strategies to prepare lanthanide MOFs including the solvothermal method, slow diffusion, and ionothermal synthesis. Different from other methods, as a facile, fast, and environmentally friend method, the ultrasonic method has been utilized to synthesize nanostructure MOFs with designable sizes,[22] and this reaction can happen because cavitations phenomena include the formation, growth, and instantaneous implosive collapse of bubbles in liquid.[23] The extreme conditions can generate local hot spots having a temperature of approximately 5000 °C, pressures of about 500 atm, and a lifetime of a few microseconds to prepare various submicron- and nanosized CPs.[24] Therefore, it is meaningful to investigate the relationship between ultrasonic conditions and the morphology of target products.

In the past few years, the abuse of antibiotics has affected peoples' daily life because it can cause pollution in different aqueous environments such as wastewater and even drinking water and groundwater.[25] It is very important to give consideration to detecting the content of antibiotics and prevent their overuse. Ornidazole, which has a chemical structure of 1-(3-chloro-2-hydroxy) propyl-2-methyl-5-nitroimidazole, is one of the 5-nitroimidazole antibiotic drugs with antibacterial and antiprotozoal activities utilized to cure anaerobic bacteria infections.[26−28] It is also utilized in the treatment of bacterial vaginosis, intestinal amoebiasis, duodenal ulcers, amoeba liver abscess, and prophylaxis during surgery.[27] The antimicrobial activity of ornidazole can be ascribed to the formation of a reactive amine group by the reduction of the nitro group, which can combine with microbial DNA and prohibit the formation of nucleic acid. Therefore, it is meaningful to detect ornidazole in a facile method.[28] Ronidazole has an antiparasitic (dinoflagellate of Turkey, trichomoniasis), antifumigative bacteria, and antibacterial effect. In particular, it is very effective to cause trichoderma in pigs.[29,30] In addition, it is also a good growth promoter, which can increase weight and improve the feed conversion rate. Current detection methods for ornidazole and ronidazole are still limited because of they are high-cost, time-consuming, and require sophisticated devices and complicated procedures.[31,32] Thus, developing fast, cost-effective, and convenient detection methods for these antibiotics in water is still interesting and quite important.

Amoeba liver abscess (ALA) will easily lead to irregular fever, night sweats, and other symptoms, and intermittent fever in the majority.[33,34] People with fever and chills often become infected with bacteria. Loss of appetite, abdominal distension, nausea, vomiting, diarrhea, dysentery, and other symptoms are common. Pain in the liver area is an important symptom of this disease, which presents as a persistent dull pain.[35] Amoebic liver abscess will easily result in clinical symptoms of fever, pain in right upper abdomen, and liver tenderness with an increased concentration of C-reactive protein (CRP) and C-reactive protein autoantibody (CRP Ab). Therefore, CRP Ab can be utilized as a biomarker for ALA.[36] If the concentration of CRP Ab is above normal in humans, it may indicate ALA. It is important and meaningful to design an excellent sensing platform to detect the biomarkers of ALA.

In this work, two unique lanthanide coordination polymers **Lu-MOF** and **Y-MOF** have been prepared through powerful solvothermal and facile ultrasonic synthetic methods. Single crystal X-ray analyses reveal that, in **Lu-MOF** and **Y-MOF**, these largely conjugated L^{3-} are linked by the lanthanide Lu^{III} and Y^{III} centers, constructing three-dimensional (3D) nanoporous frameworks. PXRD spectra revealed that powder patterns of **Lu-MOF** and **Y-MOF** are in good agreement with theoretical PXRD patterns confirming their purity. Furthermore, through the postsynthetic method,[37] fluorescent chromophores Eu^{3+} and Tb^{3+} have been introduced into **Lu-MOF** to construct a dual-emission hybrid material **Eu^{3+}/Tb^{3+}@Lu-MOF**, which can be utilized as a ratiometric fluorescent sensor for ornidazole and ronidazole with excellent sensitivity and selectivity (Scheme 1). In addition, **Y-MOF** can be utilized to combine FAM-labeled NH-ssDNA to construct the scarcely reported excellent hybrid FAM-labeled NH-ssDNA/**Y-MOF** sensing platform for CRP Ab in human serum solution, which provides an effective method for detecting biomarkers of ALA.

2. EXPERIMENTAL SECTION

2.1. General Methods. H_3L can be synthesized according to the previous literature.[38] Chemical reagents utilized in this work were purchased from commercial sources. The PerkinElmer 240 elemental analyzer is utilized to perform the C, H, and N elemental analysis. A D/Max-2500 X-ray diffractometer apparatus (Cu-Kα radiation) can be utilized to for powder X-ray diffraction (PXRD) analysis. A SB-100DT ultrasonic bath (XJ Biotechnology Instrument, Zhe Jiang, China) is utilized to perform the ultrasonic synthetic experiments. A Mepod V-1600PC spectrophotometer was used to determine the ultraviolet−visible (UV−vis) absorbance spectrum. The photo-

https://dx.doi.org/10.1021/acs.inorgchem.9b03272
Inorg. Chem. XXXX, XXX, XXX−XXX

luminescent lifetime is determined based on the fluorescence spectrophotometer (Fluorolog-3, Horiba Jobin Yvon, USA). Quantum yield was determined utilizing the FS5 fluorescence spectrometer (Edinburgh). The morphologies of **Lu-MOF and Y-MOF** nanoparticles were analyzed utilizing the ova-Nano 230 scanning electron microscope (SEM; FEI instrument, USA) with gold coating. The sequences of DNA oligonucleotides are given as

NH-ssDNA: 5′NH_2-GTACTTCCTTAAACGACGCAGG-FAM-3′

2.2. Solvothermal Synthesis of Lu-MOF and Y-MOF. *Solvothermal Synthesis of **Lu-MOF**.* A mixture containing lutetium(III) chloride (0.05 mmol, 19.5 mg), H_3L (0.05 mmol, 18.1 mg), 4 mL of DMF, and 2 mL of H_2O was placed after dissolution in a 25 mL Teflon-lined autoclave. Then the mixture was heated for 48 h at 120 °C in an oven under static conditions. Then, it was slowly cooled to ambient temperature for 48 h, the **Lu-MOF** block crystals were colorless, and the resulting products were washed with DMF and H_2O three times, respectively. The resulting crystalline powder was dried in air and collected in ca. 82% yield (on the basis of lutetium(III) chloride). Found (%): C, 43.74; H, 3.51; N, 2.13. Calcd (%): C, 44.18; H, 3.55; N, 2.15 indicating the formula for $C_{48}H_{46}Lu_2N_2O_{19}$.

*Solvothermal Synthesis of **Y-MOF**.* A mixture containing yttrium(III) chloride (0.05 mmol, 10.7 mg), H_3L (0.05 mmol, 18.1 mg), 4 mL of DMF and 2 mL of H_2O was placed after dissolution in a 25 mL Teflon-lined autoclave. Then the mixture was heated for 72 h at 120 °C in an oven under static conditions. Then, it was slowly cooled to room temperature for 48 h, and the resulting colorless block crystals **Y-MOF** were washed with DMF and H_2O three times. The resulting crystalline powder was dried in air and collected in ca. 86% yield [on the basis of yttrium(III) chloride]. Found (%): C, 51.74; H, 3.57; N, 1.95. Calcd (%): C, 52.68; H, 3.66; N, 1.98 indicating formula for $C_{23.25}H_{19.25}N_{0.75}O_{8.25}Y$.

2.3. Preparation of Lu-MOF and Y-MOF through the Ultrasonic Method. Ultrasonic syntheses of **Lu-MOF** were performed in an ultrasonic bath at room temperature and atmospheric pressure. The ultrasonic time was 80 min, and the ultrasonic power was 100 W with a 10-fold molar ratio compared to the solvothermal preparation method. The resulting powder was isolated by centrifugation, washed with DMF three times, and dried in air for further characterization.

Ultrasonic syntheses of **Y-MOF** were also performed in an ultrasonic bath at room temperature and atmospheric pressure. The ultrasonic time was 80 min and the ultrasonic power was 100 W with a 10-fold molar ratio compared to the solvothermal preparation method. The resulting powder can be isolated by centrifugation, washed with DMF three times, and dried in air for further characterization. Similar results also can be found in the previous work,[39] and $\{[Zn(L)_2(NO_3)_2]\}_n$ (1) (L = 4,4′-bis(triazol-1-ylmethyl)-biphenyl) has been synthesized through hydrothermal and sonochemical approaches. When the ultrasonic intensity increased from 70 to 100 W, the size of submicron decreased from around 5 to 1 μm, and longtime ultrasound irradiation decreased agglomeration, thus leading to the size decrease of nanoparticles.

2.4. Preparation of Eu^{3+}/Tb^{3+}@Lu-MOF through the Post-synthesis Method. Herein, 0.0030 g of **Lu-MOF** samples was added into a 30 mL mixture solution of 0.4 mM $Eu(NO_3)_3{\cdot}6H_2O$ and 0.5 mM $Tb(NO_3)_3{\cdot}6H_2O$. Then the mixed solutions was heated for 48 h at 30 °C and then cooled to room temperature. The resulting solid samples were obtained by the centrifugation for 10 min at 6000 rpm and washed with DMF three times. Then the liquid supernatant was removed, and the resulting solid samples were dried.

2.5. Methods of Solution Preparation. *2.5.1. Preparation of Antibiotic Solutions.* In this work, 0.2 mmol of sulphaguanidine, sulfathiazole, sulfamerazine, sulfadiazine, pyrazinamide, sulfisoxazole, sulfamethoxazole, thiamphenicol, chloramphenicol, ronidazole, and ornidazole was added to 10 mL of DMF to prepare a 0.02 M antibiotic solution, respectively.

2.5.2. Preparation of NH-ssDNA Sample Solution. 1 μL of 100 μM NH-ssDNA PBS buffer solution was added into a 99 μL PBS buffer solution to prepare the 1 μM NH-ssDNA solution.

2.5.3. Preparation of CRP Solution. 0.1 mmol of CRP was added into 1 mL of deionized water to prepare a 0.1 mM CRP solution.

2.5.4. Preparation of CRP Ab Solution. 0.5 mmol of CRP Ab was added into 1 mL of deionized water to prepare a 0.5 mM CRP Ab solution.

2.5.5. Preparation of Aβ's Solution. One milligram of Aβ was added into 1 mL of water, and the resulting Aβ's solution concentration was 0.943 mM. Then, 0.1 mL Aβ's solution (0.943 mM) was taken, and 0.0886 mL of deionized water was added to make 0.5 mM Aβ's solution.

2.5.6. Preparation of Thyrotropin-Releasing Hormone (TRH) Solution. 1.8 mg of TRH was added into 10 mL of deionized water to prepare a 0.5 mM TRH solution.

2.5.7. Preparation of Enkephalin (ENK) Solution. 2.778 mg of enkephalin was added into 10 mL of deionized water to prepare the 0.5 mM ENK solution.

2.5.8. Preparation of Corticotropin Releasing Factor (CRF) Solution. 0.5 mg of TRH was added into 0.1984 mL of deionized water to prepare a 0.5 mM CRF solution.

2.5.9. Preparation of Melanocyte-Stimulating Hormone Release Inhibiting Factor (MIF) Solution. 1.422 mg of MIF was added into 10 mL of deionized water to prepare a 0.5 mM MIF solution.

2.5.10. Preparation of Parathyroid Hormone (PTH) Solution. 0.5 mmol of PTH was added into 1 mL of deionized water to prepare a 0.5 mM MIF solution.

2.6. X-ray Crystallography. Single-crystal X-ray diffraction analysis for **Lu-MOF** and **Y-MOF** were determined utilizing a Bruker SMART 1000 CCD diffractometer (graphite-monochromated Cu–Kα radiation, λ = 0.71073 Å). Lorentz polarization and a ω–φ scanning strategy were utilized. Crystal structures were analyzed through the direct methods and refined with the full-matrix least-squares method utilizing the Olex2 1.2 programs. All non-hydrogen atoms were assigned by anisotropic thermal parameters. Organic hydrogen atoms were geometrically defined. Crystal data for **Lu-MOF** and **Y-MOF** are summarized in Table 1. Selected bond angles and lengths are summarized in Table S1. hydrogen bonds lengths [Å] and angles [°] calculated by PLATON program are listed in Table S2 and Table S3. These crystal data for CCDC 1946558 (**Lu-MOF**) and CCDC 1946559 (**Y-MOF**) also can be downloaded free of charge from the Cambridge Crystallographic Data Centre via www.ccdc.cam.ac.uk/data_request/cif.

Table 1. Crystallographic Data and Details of Refinements for Complexes Lu-MOF and Y-MOF[a,b]

	Lu-MOF	Y-MOF
formula	$C_{48}H_{46}Lu_2N_2O_{19}$	$C_{23.25}H_{19.25}N_{0.75}O_{8.25}Y$
M (g mol^{-1})	1304.81	530.05
crystal system	monoclinic	monoclinic
space group	C_2/c	C_2/c
a (Å)	17.7407(7)	32.897(13)
b (Å)	18.0064(5)	13.280(5)
c (Å)	35.9267(10)	13.965(6)
α (deg)	90	90
β (deg)	98.087(3)	101.308(8)
γ (deg)	90	90
V ($Å^3$)	11362.5(6)	5982(4)
Z	8	8
$F(000)$	5136.0	2152
ρ_{calc} (Mg m^{-3})	1.525	1.177
μ (mm^{-1})	3.523	1.987
data/restraints/parameters	9952/146/695	6210/136/362
GOF on F^2	1.083	1.006
R_1[a] ($I = 2\sigma(I)$)	0.0885	0.0846
ωR_2[b] (all data)	0.2494	0.2728

[a] $R_1 = \Sigma\ ||F_0| - |F_c||/|F_0|$. [b] $\omega R_2 = [\Sigma w(|F_0|^2 - |F_c^2|^2/w|F_o^2|^2]^{1/2}$.

https://dx.doi.org/10.1021/acs.inorgchem.9b03272
Inorg. Chem. XXXX, XXX, XXX−XXX

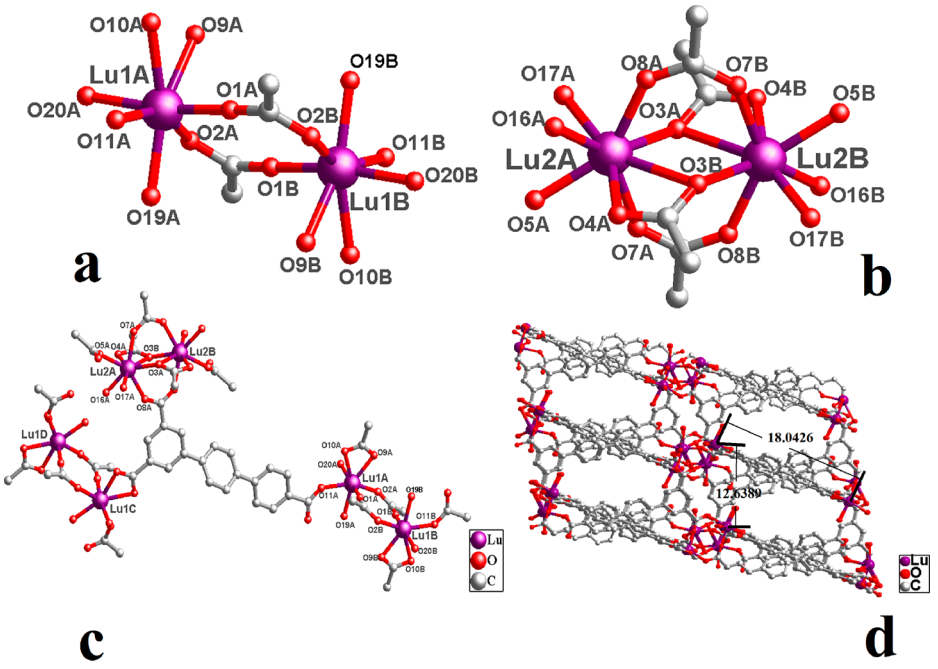

Figure 1. (a–c) Fundamental structural unit of the Lu^{III} coordination framework **Lu-MOF**; (d) 3D cluster-based nanoporous framework structure of **Lu-MOF**.

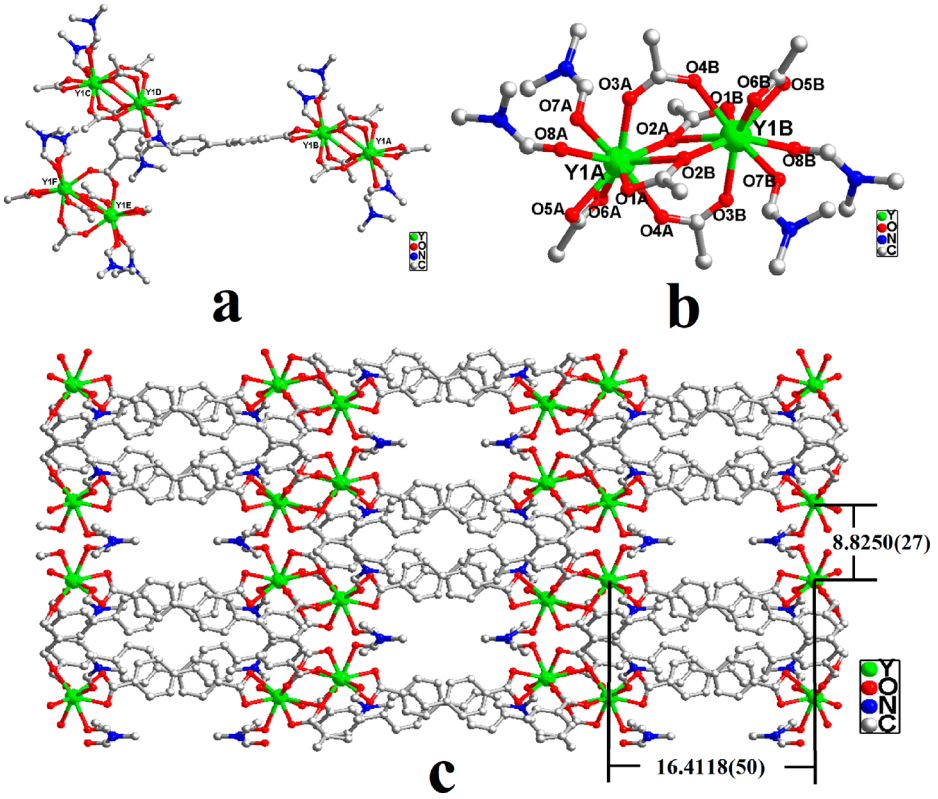

Figure 2. (a–b) Fundamental structural units of the Y^{III} coordination framework **Y-MOF**; (c) 3D cluster-based nanoporous framework structure of **Y-MOF**.

3. RESULTS AND DISCUSSION

3.1. Structure Determination of Cluster-Based Coordination Material Lu-MOF. Single-crystal diffraction analysis demonstrates (Table 1) that the **Lu-MOF** crystallizes in the monoclinic system, space group C_2/c, with the lattice parameters of a = 17.7407(7) Å, b = 18.0064(5) Å, c = 35.9267(10) Å, and cell volume 11362.5(6) $Å^3$. The asymmetric unit of **Lu-MOF** contains two crystallographically independent Lu^{III} centers (Lu1, Lu2). Lu1A and Lu1B have the same coordination pattern (Figure 1a–b). Lu1A is seven-coordinated by five O atoms (O1A, O2A, O9A, O10A, O11A) from L^{3-} and two terminal coordinated H_2O molecules

https://dx.doi.org/10.1021/acs.inorgchem.9b03272
Inorg. Chem. XXXX, XXX, XXX–XXX

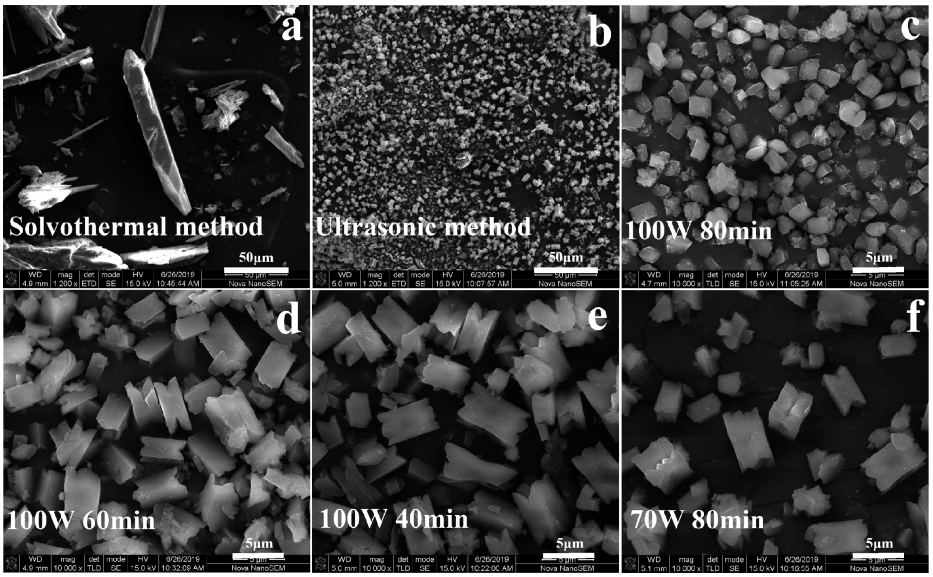

Figure 3. SEM images of **Lu-MOF** (a) under the solvothermal synthetic method; (b–f) under different ultrasonic conditions.

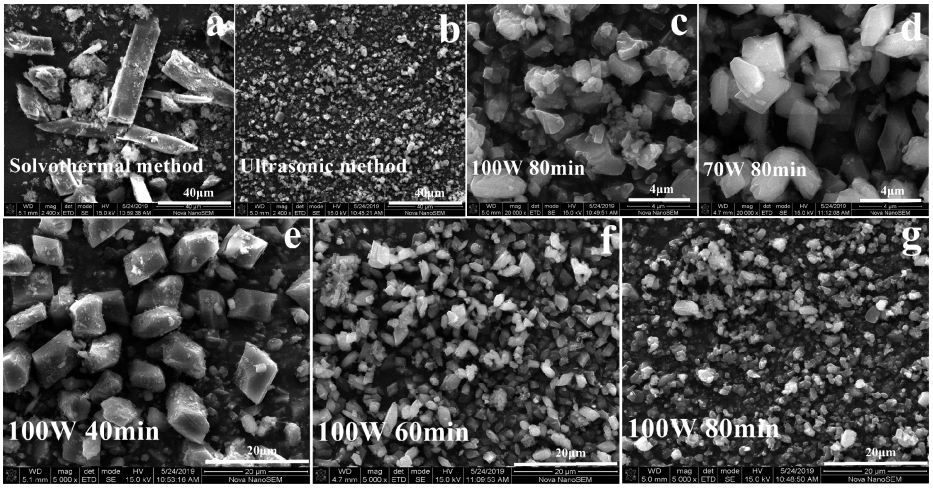

Figure 4. SEM images of **Y-MOF** (a) under the solvothermal synthetic method; (b–g) under different ultrasonic conditions.

(O19A, O20A). Two Lu1(III) centers are further connected together by two carboxylate groups of two L^{3-} to build the dinuclear eight-membered ring ($Lu_2O_4C_2$). As a secondary building unit (SBU), the distance between the centers of Lu1A and Lu1B is 4.8363 Å and the bond angle of O1A-Lu1A-O2A (O1B-Lu1B-O2B) is 103.412°, and the bond angle of O1A-C-O2B (O2A-C-O1B) is 119.310° (Figure 1a). As depicted in Figure 1b, both Lu2A and Lu2B are in the eight-coordinate mode. Lu2A is eight-coordinated by six O atoms (O3A, O4A, O5A, O7A, O8A, O3B) from L^{3-} and two terminal coordinated H_2O (O16A, O17A). Lu2A and Lu2B also form an eight-membered ring ($Lu_2O_4C_2$) through the carbon and oxygen atoms of the L^{3-} ligand. Unlike Lu1, a Lu_2O_2 four-membered ring is nested internally in the eight-membered ring to form a binuclear cage-like structure, as the secondary building unit (SBU) of Lu2. The distance between Lu2A and Lu2B is 3.835 Å, the bond angle of O8A-Lu2A-O7A (O7B-Lu2B-O8B) is 138.761°, the bond angle of Lu2A-O3A-Lu2B (Lu2A-O3B-Lu2B) is 102.208°, and O3A-Lu2A-O3B (O3A-Lu2B-O3B) is 77.792°. As depicted in Figure 1c,d, the bridging carboxylate groups link the adjacent dinuclear cluster-based SBUs to generate a 1D chain, and the neighboring chains are further interlinked by L^{3-} to construct a 3D framework containing 1D channels with a rhombus window (18.0426 Å × 12.6389 Å). On the other hand, these carbon and oxygen atoms from L^{3-} and water were also involved in C–H···O hydrogen bonds (Table S2), such weak interactions also played a crucial role in stabilizing the whole network. According to PLATON calculations, the overall potential solvent area volume is 1096.1 $Å^3$, which occupies 9.6% of the unit cell volume (11362.5 $Å^3$).

3.2. Structural Descriptions of Cluster-Based Coordination Material Y-MOF. Single-crystal diffraction analysis reveals that the cluster-based coordination material **Y-MOF** crystallizes in the monoclinic, space group C_2/c with the lattice parameters of a = 32.897(13) Å, b = 13.280(5) Å, c = 13.965(6) Å, and cell volume 5982(4) $Å^3$. There are two Y^{III} centers in the fundamental coordinated unit of **Y-MOF**, and Y1A and Y1B have the same coordination pattern (Figure 2a–b). Y1A is nine-coordinated by seven oxygen atoms (O1A, O2A, O2B, O3A, O4A, O5A, O6A) from L^{3-}, two terminal coordinated DMF (O7A, O8A). Two Y(III) centers are further

https://dx.doi.org/10.1021/acs.inorgchem.9b03272
Inorg. Chem. XXXX, XXX, XXX–XXX

connected together by two carboxylate of two L^{3-} to build the dinuclear eight-membered ring ($Y_2O_4C_2$). It should be noticed that the Y_2O_2 four-membered ring is internally nested in eight-membered ring to form a binuclear cage-like structure, as the secondary building unit (SBU) of **Y-MOF**. The distance between the centers of Y1A and Y1B is 3.9666(14) Å, the bond angle of O3A-Y1A-O4A (O4B-Y1B-O3B) is 132.527°, the bond angle of Y1A-O2A-Y1B (Y1A-O2B-Y1B) is 105.104°, and O2A-Y1A-O2B (O2A-Y1B-O2B) is 74.896°. As depicted in Figure 2c, the bridging carboxylate groups also join the adjacent dinuclear cluster-based SBUs to generate a 1D chain, and the neighboring chains are further interlinked by L^{3-} to construct a 3D framework containing 1D channels with a rectangle window (16.412 Å × 8.8250 Å). On the other hand, these carbon and oxygen atoms from L^{3-} and water were also involved in C−H···O hydrogen bonds (Table S2). Such weak interactions also played a crucial role in stabilizing the whole network. PLATON calculation reveals the overall potential solvent area volume is 742.8 $Å^3$, which occupies 12.4% of the unit cell volume (5983 $Å^3$).

3.3. Nanobulk Size and Morphology of Lu-MOF and Y-MOF. As **Lu-MOF** and **Y-MOF** can be obtained by the ultrasonic method, a discussion on the relationship between ultrasonic preparation conditions, nanosize, and morphology should be given. For **Lu-MOF**, according to the scanning electron microscopy (SEM) images (Figure 3a−b), **Lu-MOF** nanobulk sizes vary from 10 to 152 μm under the solvothermal method and different ultrasonic conditions, respectively. As for the **Y-MOF** (Figure 4a−b), **Y-MOF** nanobulk sizes can be observed to vary from 5 to 130 μm under the solvothermal method and different ultrasonic conditions, respectively. Nanoballs of **Lu-MOF** can be obtained for different sonication times (40 min, 60 min, 80 min) at an ultrasonic power of 100 W, and nanobulks of **Lu-MOF** can be synthesized under the sonication power (70 W) and sonication time (80 min).[39−45]

As depicted in Figure 4a, the crystals fabricated by solvothermal synthesis were observed in that they are not well separated and are much larger than these **Lu-MOF** and **Y-MOF** materials generated by different ultrasonic conditions. The particle sizes and morphology of nanoparticles rely on different sonication times. As depicted in Figure 3c−e and Figure 4c−f, the results showed that smaller sheets can be obtained when the sonication time is prolonged. Moreover, as shown in Figure 3c, Figure 3f, Figure 4c, and Figure 4d, smaller blocks were fabricated when the sonication power increased. The results reveal that the sonication time and sonication power can deliberately influence and tune the sizes and morphologies of **Lu-MOF** and **Y-MOF** products.

3.4. Solid Fluorescent Spectrum, Energy Transfer, TG Analysis and Combination Mode in Eu^{3+}/Tb^{3+}@Lu-MOF. The 1D nanoporous channel between the neighboring Lu···Lu separation of 12.6743(10) × 9.0175(6) Å also can be observed in the **Lu-MOF** framework (Figure 1d), which also provides the possibility that Eu^{3+} and Tb^{3+} can easily enter the framework's channel. The solid fluorescent emission spectra of **Eu^{3+}/Tb^{3+}@Lu-MOF** are presented in Figure 5. It is noted that in synthesis, though two kinds of MOF samples (crystals and crystalline powders) are obtained, these materials should be the same, which also has been identified by PXRD patterns in Figure 6. It is noted that **Eu^{3+}/Tb^{3+}@Lu-MOF** demonstrates Tb^{3+} characteristic transitions at 488, 545, 583 nm, respectively, and **Eu^{3+}/Tb^{3+}@Lu-MOF** demonstrates Eu^{3+} characteristic transitions at 580, 593, 615 nm, respectively.

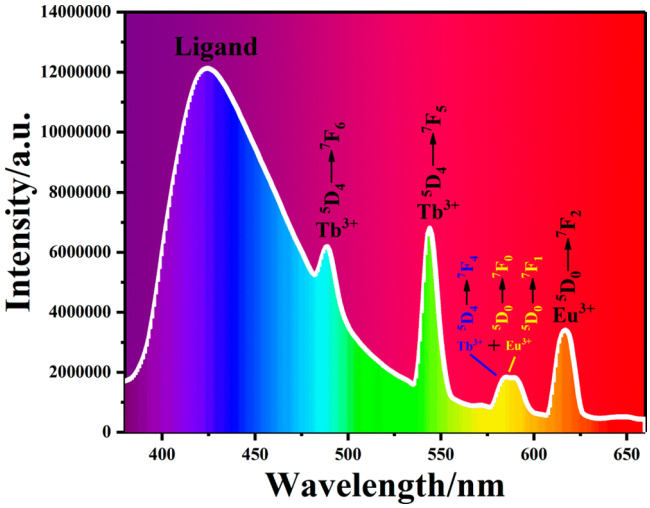

Figure 5. Solid fluorescent spectrum of **Eu^{3+}/Tb^{3+}@Lu-MOF**.

When **Eu^{3+}/Tb^{3+}@Lu-MOF** is irradiated at 290 nm, its emission bands are very consistent with the characteristic peaks of Tb^{3+} and Eu^{3+}. Its two dominant peaks at 615 and 593 nm are correlated with $^5D_0$-^7F_J (J = 0, 1, 2) transitions of Eu^{3+}, and the other weaker peaks at 488 and 545 nm are correlated with $^5D_4$-^7F_J (J = 5, 6) transitions of Tb^{3+}. Its remaining emission peaks around 580 can be ascribed to $^5D_0$-^7F_J (J = 0, 1) transitions of Eu^{3+}.

Thermogravimetric decay analysis (TGA) curve of **Lu-MOF** and **Y-MOF** also have been recorded (Figure S1). The weight loss of **Lu-MOF** and **Y-MOF** materials ranging from 30 to 200 °C are 13.47 and 11.66 wt %, respectively, which should be attributed to the weight loss for coordination water, free DMF, and coordination DMF molecules. These results can be in good agreement with the calculated values (12.63 and 10.34 wt %, respectively).

Although solvent water molecules may quench lanthanide emission, **Eu^{3+}/Tb^{3+}@Lu-MOF** can be sensitized by H_3L through the antenna effect. As is shown in Figure S2, upon irradiation with ultraviolet radiation, the organic ligands of the lanthanide complex are excited to a vibrational level of the first excited singlet state (S_0 to S1 energy level), and then through intersystem crossing,[46] the complex should undergo a nonradiative transition from the triplet state to an excited state of the lanthanide ion. After this indirect excitation by energy transfer, the lanthanide ion may undergo a radiative transition to a lower 4f state by characteristic line-like photoluminescence.

To test the depth range distribution of rare earth ions at a more microscale level, high-resolution transmission electron microscopy-energy dispersive spectra (TEM-EDS) analysis is applied to determine the **Eu^{3+}/Tb^{3+}@Lu-MOF** hybrid material. From the EDS mappings (Figure 7), Eu^{3+} and Tb^{3+} are distributed in the **Lu-MOF** framework, which indicates that Eu^{3+} and Tb^{3+} are located in channels of the **Lu-MOF** framework. To further confirm Eu^{3+} and Tb^{3+} can be accommodated into the channels of the **Lu-MOF** framework, the solvent-absorption experiment was employed. By soaking the sample of **Eu^{3+}/Tb^{3+}@Lu-MOF** in the acetone solvent for 24 h at room temperature, the sorption of *p*-hydroxybenzaldehyde by the activated **Eu^{3+}/Tb^{3+}@Lu-MOF** was also investigated, which can be monitored by UV/vis absorption spectroscopy. By immersing **Eu^{3+}/Tb^{3+}@Lu-MOF** in *p*-

https://dx.doi.org/10.1021/acs.inorgchem.9b03272
Inorg. Chem. XXXX, XXX, XXX−XXX

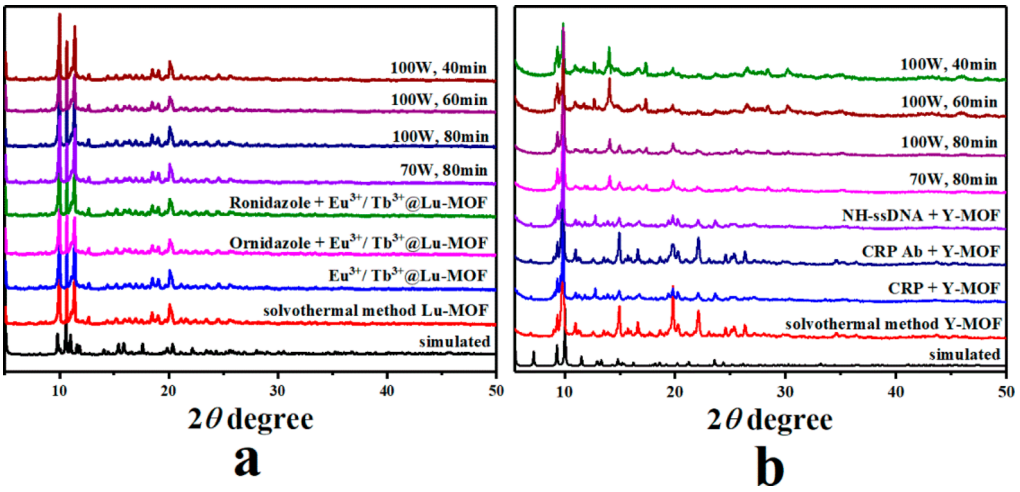

Figure 6. (a) Experimental PXRD patterns of **Lu-MOF** under different ultrasonic conditions and in different solutions. (b) Experimental PXRD patterns of **Y-MOF** under different ultrasonic conditions and in different solutions.

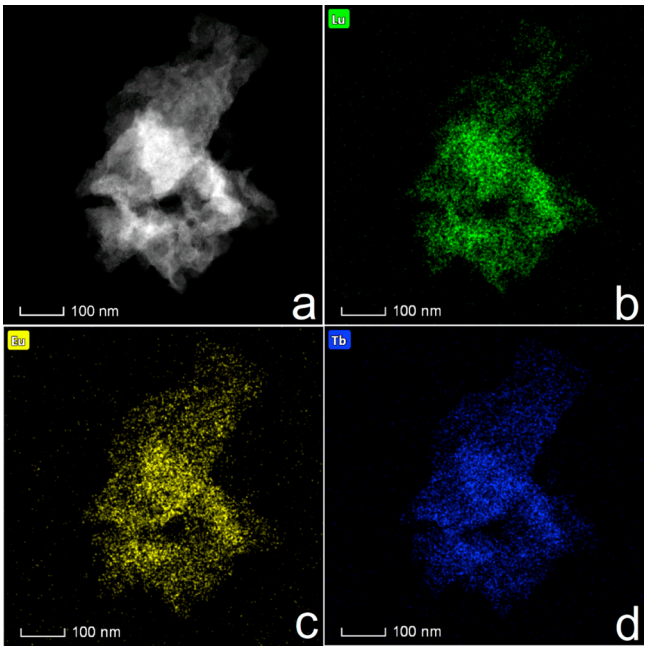

Figure 7. (a–d) EM images and mapping of **Eu^{3+}/Tb^{3+}@Lu-MOF**.

hydroxybenzaldehyde for 12 h at room temperature, UV/vis analysis indicates that 0.25 molecule of *p*-hydroxybenzaldehyde per formula unit can be absorbed (Figure S3), and the solvent-uptake was 2.31 wt %. The result also reveals that **Eu^{3+}/Tb^{3+}@Lu-MOF** has the ability to further accommodate such large *p*-hydroxybenzaldehyde molecule, which also reveals that small Eu^{3+} and Tb^{3+} ions should be introduced into the channel of **Lu-MOF**. The result may be somewhat similar to the previously reported Dye@CZJ-3 platform (CZJ-3 = [CdL-(H_2O)]·4DMF·$2H_2O$, L= (*E*)-4-(2-carboxyvinyl)benzoic acid),[47] in which the microporous channel of CZJ-3 is also confirmed by the absorption experiments for aromatic benzyl alcohol solvents utilizing the UV–vis spectrum.

3.5. Selectivity and Sensitivity of Ratiometric Fluorescent Sensor Eu^{3+}/Tb^{3+}@Lu-MOF for Detecting Ornidazole and Ronidazole. Ornidazole and ronidazole as antibiotics can be used effectively for ALA and trichoderma in pigs. However, when these antibiotics are overused, it will result in massive accumulation of antibiotics in food and animals because most antibiotics do not easily degrade in nature. Most antibiotics enter the human body via wastewater or food polluted by wastewater, which also leads to intricate environmental pollution.[48] Designing a fluorescent sensor to detect ornidazole and ronidazole will help us to investigate their amount, which can further prevent the abuse of these antibiotics.

First, to test the selectivity of **Eu^{3+}/Tb^{3+}@Lu-MOF** in the antibiotics detection process, we designed the following experiment: 0.02 mM antibiotics solutions (including sulphaguanidine, sulfathiazole, sulfamerazine, sulfadiazine, pyrazinamide, sulfisoxazole, sulfamethoxazole, thiamphenicol, chloramphenicol, ronidazole, ornidazole) were added into an **Eu^{3+}/Tb^{3+}@Lu-MOF** suspension (0.1 g/L, 3 mL, samples synthesized by the solvent method), respectively. Different from other antibiotics, ornidazole and ronidazole can influence the intensity of **Eu^{3+}/Tb^{3+}@Lu-MOF** distinctly with both emissions at 545 and 616 nm (Figure 8). Therefore, **Eu^{3+}/Tb^{3+}@Lu-MOF** can be utilized as an excellent sensor for ornidazole and ronidazole.

Second, to determine the sensitivity of **Eu^{3+}/Tb^{3+}@Lu-MOF** for ornidazole, when different concentrations of ornidazole varying from 0 to 1.2 μM are added into **Eu^{3+}/**

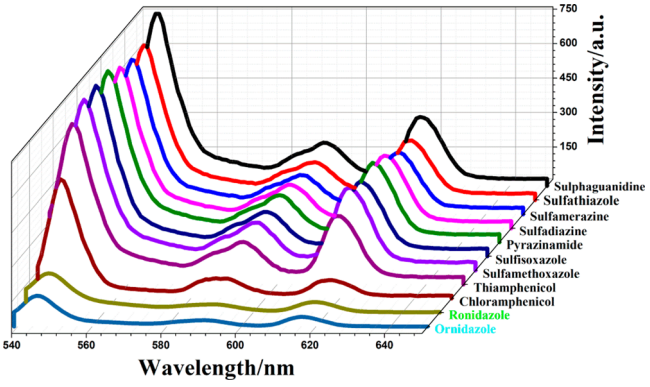

Figure 8. Fluorescence emission spectra of **Eu^{3+}/Tb^{3+}@Lu-MOF** (0.1 g/L, 3 mL) by the addition of different antibiotics molecule solutions (50 μM) when excited at 350 nm.

https://dx.doi.org/10.1021/acs.inorgchem.9b03272
Inorg. Chem. XXXX, XXX, XXX–XXX

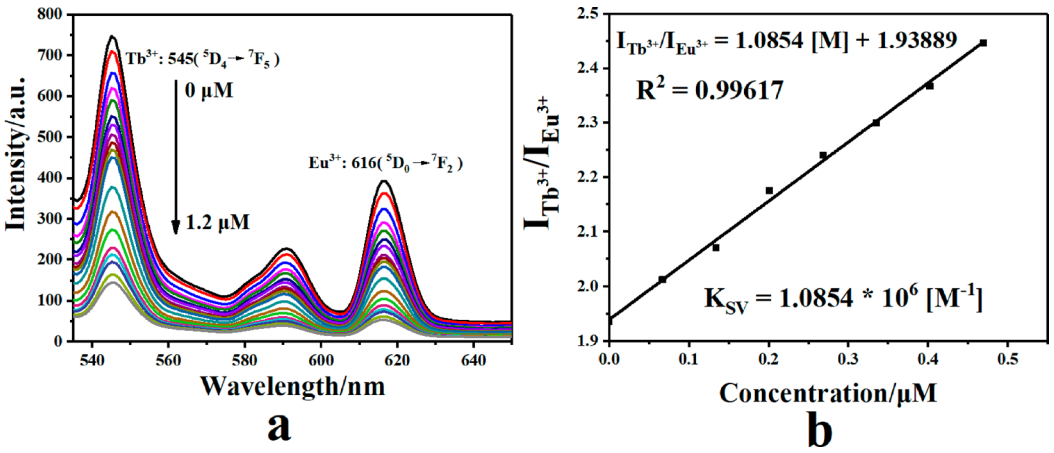

Figure 9. (a) Fluorescence emission spectra of **Eu^{3+}/Tb^{3+}@Lu-MOF** (0.1 g/L, 3 mL) by the addition of different concentrations of ornidazole solution when excited at 350 nm; (b) the linear relation between the fluorescence intensity ratio and different concentrations of ornidazole solution added into **Eu^{3+}/Tb^{3+}@Lu-MOF**.

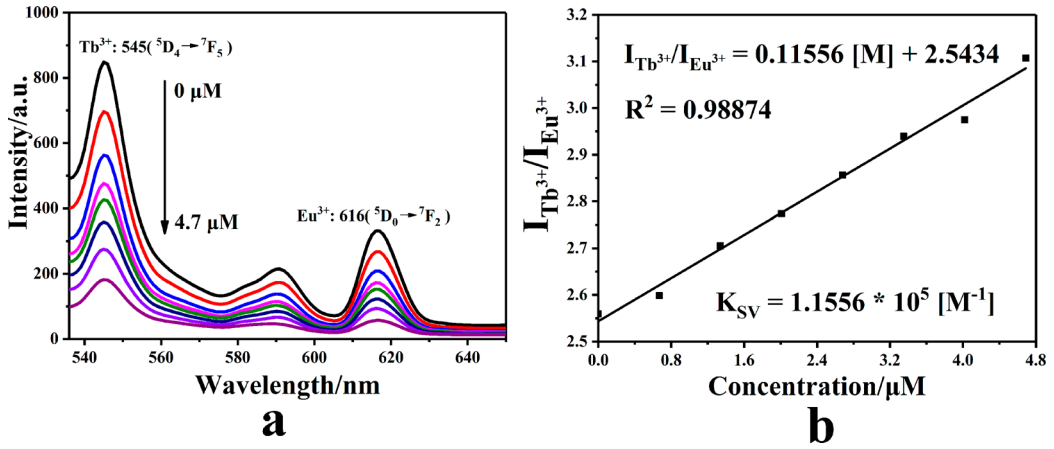

Figure 10. (a) Fluorescence emission spectra of **Eu^{3+}/Tb^{3+}@Lu-MOF** (0.1 g/L, 3 mL) by the addition of different concentrations of ronidazole solutions when excited at 350 nm; (b) the linear relation between the fluorescence intensity ratio of **Eu^{3+}/Tb^{3+}@Lu-MOF** under different concentrations of ronidazole solutions.

Tb^{3+}@Lu-MOF, the fluorescent intensities gradually decrease (Figure 9a). The fluorescence quenching efficiency was calculated using the following equation: $I_{Tb}/I_{Eu} = K_{sv}[M] + C$, where K_{sv} is the quenching constant (M^{-1}), [A] is the molar concentration of the analyte, and I_{Tb} and I_{Eu} are the fluorescence intensities after the addition of analyte, respectively. The K_{sv} value for ornidazole is 1.0854×10^6 [M^{-1}], and the low of detection (LOD) should be obtained by following equation: $LOD = 3S_0/S$ (S_0 is the standard deviation for the blank, S is the slope of calibration curve, $S/N = 3$) is 2.85 nM (Figure 9b), which is far more sensitive than other fluorescent sensors.[49,50] Therefore, **Eu^{3+}/Tb^{3+}@Lu-MOF** can be utilized as an excellent sensor for ornidazole with high sensitivity. On the other hand, we also investigated that the sensitivity of sample suspensions under different ultrasonic conditions to detect ornidazole (Figure S4). There was a relatively poor linear relationship between the ornidazole concentration and the fluorescent ratio of **Eu^{3+}/Tb^{3+}@Lu-MOF** in comparison with these nanoparticles synthesized under the solvothermal method. Therefore, **Eu^{3+}/Tb^{3+}@Lu-MOF** (under solvothermal method) can be utilized as an excellent sensor for ornidazole.

Third, to determine the sensitivity of **Eu^{3+}/Tb^{3+}@Lu-MOF** for ronidazole, when different concentrations of ronidazole varying from 0 to 4.7 μM are added into **Eu^{3+}/Tb^{3+}@Lu-MOF**, the fluorescent intensities also gradually decreased (Figure 10a). The fluorescence quenching efficiency was calculated using the following equation: $I_{Tb}/I_{Eu} = K_{sv}[M] + C$, where K_{sv} is the quenching constant (M^{-1}), [A] is the molar concentration of the analyte, and I_{Tb} and I_{Eu} are the fluorescence intensities after the addition of analyte, respectively. The K_{sv} value for ronidazole is 1.1556×10^5 [M^{-1}] (Figure 10b), and the detection limit is 26.7 nM, which can be compared with other sensitive fluorescent sensors.[51,52] Therefore, **Eu^{3+}/Tb^{3+}@Lu-MOF** also can be utilized as an excellent sensor for ronidazole with high sensitivity. On the other hand, we also investigated the sensitivity of sample suspensions under different ultrasonic conditions to detect ronidazole (Figure S5). There was a poor linear relationship between the concentration of ronidazole and the fluorescent ratio of **Eu^{3+}/Tb^{3+}@Lu-MOF** in comparison with these nanoparticles synthesized under the solvothermal method. Therefore, **Eu^{3+}/Tb^{3+}@Lu-MOF** (under solvothermal method) can be utilized as an excellent sensor for ronidazole.

In addition, **Eu^{3+}/Tb^{3+}@Lu-MOF** can detect ornidazole and ronidazole, which also have a high detection sensitivity among the mixed antibiotic solutions. As depicted in Figure S6, when different concentrations containing the mixed antibiotics such

https://dx.doi.org/10.1021/acs.inorgchem.9b03272
Inorg. Chem. XXXX, XXX, XXX−XXX

as ornidazole, sulphaguanidine, sulfathiazole, sulfamerazine, sulfadiazine, pyrazinamide, sulfisoxazole, sulfamethoxazole, thiamphenicol, and chloramphenicol solutions are added into the **Eu^{3+}/Tb^{3+}@Lu-MOF** suspension, the fluorescence intensities of **Eu^{3+}/Tb^{3+}@Lu-MOF** could be easily influenced. The new linear relationship between ornidazole concentration and **Eu^{3+}/Tb^{3+}@Lu-MOF** intensity is I_{Tb}/I_{Eu} = 8.28357 [M] + 1.90209. The calculated K_{sv} value is 8.2835 × 10^6 [M^{-1}], which indicates that the **Eu^{3+}/Tb^{3+}@Lu-MOF** sensor can effectively detect ornidazole and avoid other antibiotic interference in mixed solutions. However, as depicted in Figure S7, **Eu^{3+}/Tb^{3+}@Lu-MOF** also can detect ronidazole in mixed antibiotic solutions. For details, when different concentrations of mixed antibiotics containing ronidazole sulphaguanidine, sulfathiazole, sulfamerazine, sulfadiazine, pyrazinamide, sulfisoxazole, sulfamethoxazole, thiamphenicol, and chloramphenicol solutions were added into a **Eu^{3+}/Tb^{3+}@Lu-MOF** suspension, the fluorescence intensity of **Eu^{3+}/Tb^{3+}@Lu-MOF** could be easily influenced. The new linear relationship between ronidazole concentration and intensity of **Eu^{3+}/Tb^{3+}@Lu-MOF** is I_{Tb}/I_{Eu} = 10.59549 [M] + 1.65904. The calculated K_{sv} value is 1.0595 × 10^7 [M^{-1}], which indicates that the **Eu^{3+}/Tb^{3+}@Lu-MOF** sensor can effectively detect ronidazole.

3.6. Selectivity and Sensitivity of Excellent Sensing Platform Y-MOF for Detecting CRP Ab. ALA will easily result in the clinical symptoms fever, pain in right upper abdomen, and liver tenderness with an increased concentration C-reactive protein (CRP) and C-reactive protein autoantibody (CRP Ab). Through investigating the concentration of CRP Ab, ALA can be monitored by CRP Ab, which acts as a biomarker for ALA, to detect CRP Ab with high sensitivity, The protein−aptamer binding strategy should be taken: (1) The aptamer for CRP Ab, namely, ssDNA, is a DNA sequence with specific binding with CRP Ab; (2) because CRP Ab did not have any fluorescent chromophore, 5-carboxyfluorescein (FAM) is modified by aptamer, which can be investigated on a fluorescent spectrum; (3) to further improve the sensitivity of the CRP Ab detection process, the amino group was modified by 3′-ssDNA to fabricate NH-ssDNA, which easily strengthens hydrogen-bonding interactions with **Y-MOF** and CRP; (4) **Y-MOF** is utilized as a highly sensitive sensing platform, which attracted CRP, CRP Ab, and NH-ssDNA through hydrogen-bonding interactions (Scheme 2).

Herein, 0.1 μM NH-ssDNA buffer solution was added into the **Y-MOF** suspension solution (0.1 g/L, 2.995 mL, human serum solution 0.5 μL), and then the mixed solutions were kept for 10 min until the fluorescent intensity of FAM-labled NH-ssDNA was stable. Then CRP Ab and some CRP Ab's analogue proteins (such as thyrotropin-releasing hormone (TRH), enkephalin (ENK), corticotropin releasing factor (CRF), melanocyte-stimulating hormone release inhibiting factor (MIF), β-amyloid (Aβ), parathyroid hormone (PTH)) were added in the detection system, respectively. Different from other proteins, NH-ssDNA's fluorescent intensity only can be influenced dramatically by CRP Ab (Figure 11). Therefore, **Y-MOF**/NH-ssDNA is the scarcely reported hybrid MOFs-based sensing platform that behaved with high selectivity for CRP Ab.

Although FAM-labeled NH-ssDNA have an emission peak located at 525 nm, when different concentrations of CRP Ab are directly added into the solutions only containing FAM labled NH-ssDNA, FAM-labled NH-ssDNA's fluorescent intensity gradually decrease. However, only an irregular

Scheme 2. Illustration of the CRP Ab Detection Process by the Hybrid FAM-Labeled NH-ssDNA/Y-MOF Sensing Platform

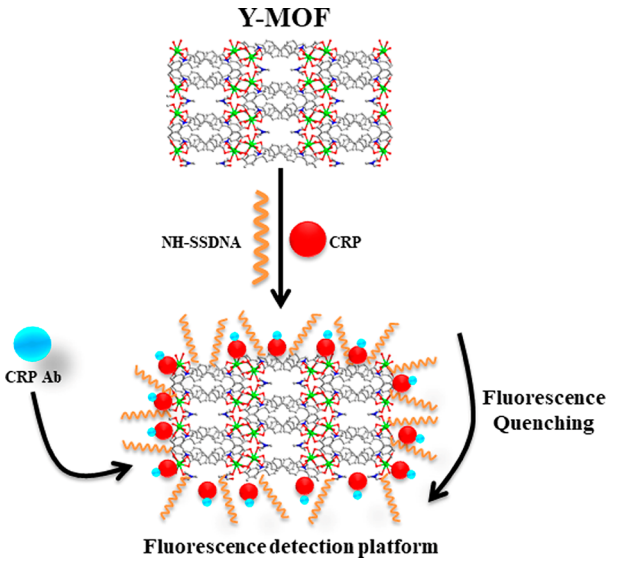

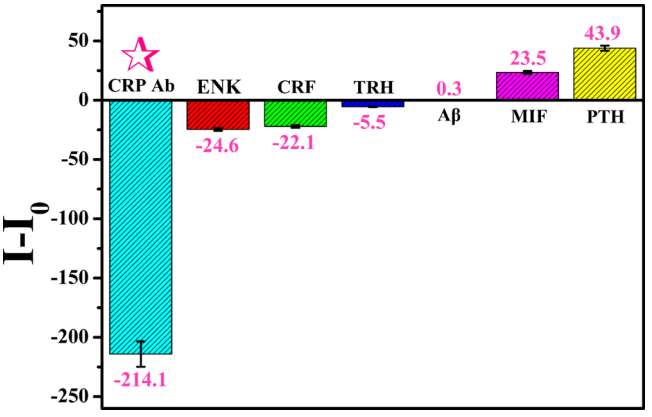

Figure 11. Fluorescent intensity variable values ($I - I_0$) when **Y-MOF** is added to different CRP Ab and some CRP Ab's analogue proteins (I_0 and I represent the fluorescent intensity of **Y-MOF** before and after adding CRP Ab and some CRP Ab's analogue proteins).

relationship between CRP Ab concentration and NH-ssDNA fluorescent ratio can be obtained (I_0/I = 0.03015x + 1.0366, R^2 = 0.83244) (Figure S8). Therefore, improving the sensitivity of the NH-ssDNA sensing platform should be considered. Herein, after CRP Ab was added into the mixture solution of **Y-MOF** and 0.5 mM CRP solution, a new excellent linear relationship between CRP Ab concentration and NH-ssDNA fluorescent ratio was obtained (I_0/I = 0.34611x + 1.03892, R^2 = 0.99401) the K_{sv} value is 3.4661 × 10^5 [M^{-1}] (Figure 12). Therefore, the result also reveals that, through the protein−aptamer binding strategy, **Y-MOF** sensing platform's sensitivity for CRP Ab was improved. The sensing performance improvement by **Y-MOF** and CRP may be because CRP may have specific protein−aptamer binding with CRP Ab, which can lead to a further quenching effect through the strength of the hydrogen-bond interactions. On the other hand, we also investigated the sensitivity of sample suspensions under different ultrasonic conditions to detect CRP Ab (Figure S9). There was a relatively poor linear relationship between the concentration of CRP Ab and the fluorescent intensity of **Y-**

https://dx.doi.org/10.1021/acs.inorgchem.9b03272
Inorg. Chem. XXXX, XXX, XXX−XXX

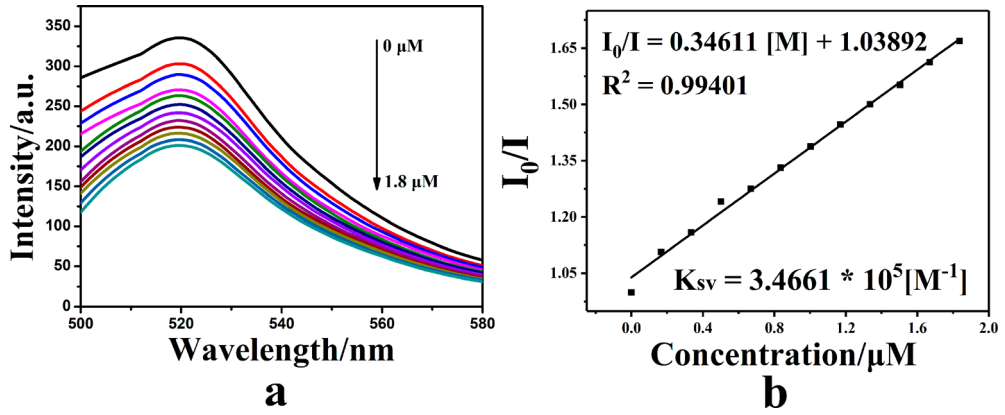

Figure 12. (a) Fluorescent spectrum of NH-ssDNA after adding different concentrations of CRP Ab in 2.5 nM CRP; (b) fluorescent ratio of NH-ssDNA after adding different concentrations of CRP Ab in 2.5 nM CRP.

Table 2. Fluorescent Lifetime of Eu^{3+}/Tb^{3+}@Lu-MOF in Different Solutions

sample	B_1	T_1/ns	B_2	T_2/ns	combined life rating/ns
Eu^{3+}/Tb^{3+}@Lu-MOF	299.16058	110.9289895	2.32×10^6	7.6833058	7.88
Eu^{3+}/Tb^{3+}@Lu-MOF + ornidazole	1.07×10^6	8.8809442	220.54689	146.5776341	9.35
Eu^{3+}/Tb^{3+}@Lu-MOF + ronidazole	648599.216	9.7096212	234.48193	143.2286709	10.42

MOF in comparison with these nanoparticles synthesized under the solvothermal method. Therefore, **Y-MOF** (under the solvothermal method) can be utilized as an excellent sensing platform for CRP Ab.

3.7. Sensing Mechanism for the Ornidazole and Ronidazole via Eu^{3+}/Tb^{3+}@Lu-MOF. To explore the sensing mechanism for the highly sensitive discrimination toward ornidazole and ronidazole by **Eu^{3+}/Tb^{3+}@Lu-MOF**, some experiments such as PXRD, UV−vis, and fluorescent lifetime in the detection process also have been investigated: (1) First, PXRD was performed, and the results showed that **Eu^{3+}/Tb^{3+}@Lu-MOF** still retained its crystal state after fluorescence detection of ornidazole and ronidazole, respectively (Figure 6a). The result also indicates that the hybrid material remained intact after the addition of ornidazole and ronidazole. (2) Second, there should exist a fluorescence resonance energy transfer (FRET) between ornidazole and **Eu^{3+}/Tb^{3+}@Lu-MOF**,[53] which also can be verified by fluorescent lifetime variation of **Eu^{3+}/Tb^{3+}@Lu-MOF** (Figure S10). When ornidazole is added into **Eu^{3+}/Tb^{3+}@Lu-MOF** suspension, the fluorescence lifetime of **Eu^{3+}/Tb^{3+}@Lu-MOF** varied from 7.88 to 9.35 ns, which also indicated that the fluorescent lifetime of **Eu^{3+}/Tb^{3+}@Lu-MOF** increased after the detection of antibiotic molecules (Figure S10). On the other hand, in the ronidazole's detection process, fluorescent lifetime variation of **Eu^{3+}/Tb^{3+}@Lu-MOF**s is from 7.88 to 10.42 ns (Table 2), which also confirm that FRET happens in this detection process. Similar results can be found in the previous work.[52] Ma's group found that through the ion-exchange method, one dual-emitting indium-organic framework **1**⊃DSM was prepared with the encapsulation of cationic dye 4-[*p*-(dimethylamino)styryl]-1-ethylpyridinium (DSM), **1**@DSM has a broad response to nitroimidazole-based antibiotics (including ornidazole and ronidazole) at low concentrations; (3) In addition, the orbital energy theoretical calculation and UV−vis absorption experiments confirmed that the quenching performances could be mainly attributed to the electron transfer and resonance energy transfer effect between the framework and the analytes. Overall, in the ornidazole and ronidazole's detection process, there should exist the photo-induced electron transfer and energy transfer mechanism because the electron-rich **Lu-MOF** containing large conjugated moieties should have the good charge transfer ability to the electron-deficient nitro-antibiotics.

3.8. Sensing Mechanism for the CRP Ab via Y-MOF. To understand the detection process of CRP Ab via Y-MOF, a possible mechanism should be considered: (1) PXRD patterns show that **Y-MOF**'s framework remains stable after the **Y-MOF** sample is soaked in a mixture of NH-ssDNA and CRP and CRP Ab (Figure 6b); (2) NH-ssDNA does not have any fluorescent chromophores, while FAM-labeled NH-ssDNA has an emission peak that is located at 525 nm. Because **Y-MOF** has the strong conjugated structure, it will easily combine with NH-ssDNA through hydrogen-bonding interactions. In addition, NH-ssDNA can specifically bind with CRP and CRP Ab through hydrogen bonding interactions, which leads to a quenching effect in the detection process;[38] (3) As shown in Figure S11, the characteristic absorption bands for the DMF acylamino group in **Y-MOF** can be observed in the FT-IR spectrum, which are located around 3400 cm^{-1}. When CRP Ab was added into the mixture containing **Y-MOF**, CRP, and NH-ssDNA, the characteristic absorption bands will gradually turn red-shift, absorption intensity become stronger, the result should be ascribed that the N−H and O−H bond length grows longer because acylamino group's vibrational dipole distances become larger. Therefore, hydrogen-bond interactions between the **Y-MOF** surface, **NH-ssDNA**, CRP, and CRP Ab can lead to a further quenching effect in the detection process of CRP Ab. These results were similar to recent work, in which the MIL-101 framework is applied as a fluorescence DNA platform;[54] (4) According to the TEM images, ACP and ACP Ab can be observed around **Y-MOF**, which indicates this detection process happens on the surface of **Y-MOF** (Figure 13). Overall, **Y-MOF** can behave as an excellent sensing platform for CRP Ab through hydrogen-bonding interactions.

https://dx.doi.org/10.1021/acs.inorgchem.9b03272
Inorg. Chem. XXXX, XXX, XXX−XXX

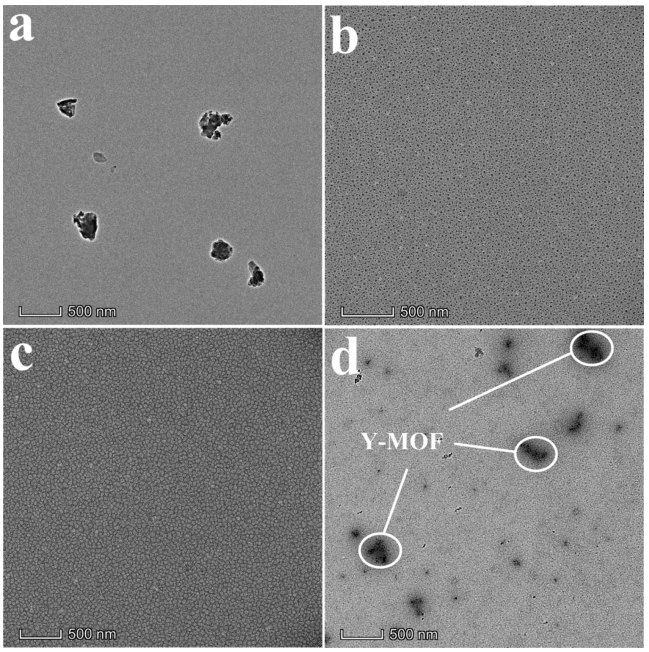

Figure 13. TEM images of (a) **Y-MOF**, (b) CRP and CRP Ab, (c) NH-ssDNA, (d) the mixture of **Y-MOF** and CRP and CRP Ab.

4. CONCLUSION AND PROSPECTS

In this work, through the solvothermal and facile ultrasonic method, two unique cluster-based lanthanide Lu and Y coordination materials $\{[Lu_2(L)_2]\cdot 2DMF\cdot H_2O\}_n$ (**Lu-MOF**) and $[Y(L)(DMF)_{0.75}]_n$ (**Y-MOF**) have been synthesized. Herein, through a postsynthesis assembly strategy, Eu^{3+} and Tb^{3+} cations are introduced into **Lu-MOF** to construct a ratiometric sensor **Eu^{3+}/Tb^{3+}@Lu-MOF**, which can successfully be utilized to discriminate ornidazole and ronidazole with a low detection limit and excellent quenching efficiency. In addition, **Y-MOF** also has been successfully designed to combine FAM-labeled NH-ssDNA to construct the scarcely reported excellent hybrid FAM-labeled NH-ssDNA/**Y-MOF** sensing platform, which can be utilized for the detection of amoeba liver abscess biomarker-CRP Ab with excellent selectivity and sensitivity. Additionally, through deliberately adjusting the ultrasonic irradiation time and power, Lu- and Y-MOFs with different sizes and morphologies can be obtained, which can provide an effective method to fabricate these lanthanide MOFs. This work also provides potential synthesis strategies for preparing the dual-emission ratiometric fluorescent sensor. These MOFs-based fluorescent sensing platforms can be expected to detect different target biomarkers; it will be helpful to explore the correlation effect between other biomarkers and these MOFs-based sensing platforms.

■ ASSOCIATED CONTENT

Supporting Information

The Supporting Information is available free of charge at https://pubs.acs.org/doi/10.1021/acs.inorgchem.9b03272.

Selected bonds and angles, hydrogen bonds for **Lu-MOF** and **Y-MOF**, the fluorescent lifetime of **Eu^{3+}/Tb^{3+}@Lu-MOF** in different solutions (PDF)

Accession Codes

CCDC 1946558−1946559 contain the supplementary crystallographic data for this paper. These data can be obtained free of charge via www.ccdc.cam.ac.uk/data_request/cif, or by emailing data_request@ccdc.cam.ac.uk, or by contacting The Cambridge Crystallographic Data Centre, 12 Union Road, Cambridge CB2 1EZ, UK; fax: +44 1223 336033.

■ AUTHOR INFORMATION

Corresponding Authors

Xin Rui Wang − *Key Laboratory of Inorganic-Organic Hybrid Functional Material Chemistry (Tianjin Normal University), Ministry of Education, Tianjin Key Laboratory of Structure and Performance for Functional Molecule, College of Chemistry, Tianjin Normal University, Tianjin 300387, PR China;* orcid.org/0000-0002-3085-5697; Email: wangxinrui-tjnu@outlook.com

Bin Ding − *Key Laboratory of Inorganic-Organic Hybrid Functional Material Chemistry (Tianjin Normal University), Ministry of Education, Tianjin Key Laboratory of Structure and Performance for Functional Molecule, College of Chemistry, Tianjin Normal University, Tianjin 300387, PR China; Key Laboratory of Advanced Energy Materials Chemistry (Ministry of Education), Collaborative Innovation Center of Chemical Science and Engineering (Tianjin), College of Chemistry, Nankai University, Tianjin 300071, PR China;* orcid.org/0000-0001-7973-3183; Email: hxxydb@mail.tjnu.edu.cn

Authors

Xing Ze Wang − *Key Laboratory of Inorganic-Organic Hybrid Functional Material Chemistry (Tianjin Normal University), Ministry of Education, Tianjin Key Laboratory of Structure and Performance for Functional Molecule, College of Chemistry, Tianjin Normal University, Tianjin 300387, PR China*

Xin Yu Mao − *Key Laboratory of Inorganic-Organic Hybrid Functional Material Chemistry (Tianjin Normal University), Ministry of Education, Tianjin Key Laboratory of Structure and Performance for Functional Molecule, College of Chemistry, Tianjin Normal University, Tianjin 300387, PR China*

Zi Qing Zhang − *Key Laboratory of Inorganic-Organic Hybrid Functional Material Chemistry (Tianjin Normal University), Ministry of Education, Tianjin Key Laboratory of Structure and Performance for Functional Molecule, College of Chemistry, Tianjin Normal University, Tianjin 300387, PR China*

Rui Guo − *Key Laboratory of Inorganic-Organic Hybrid Functional Material Chemistry (Tianjin Normal University), Ministry of Education, Tianjin Key Laboratory of Structure and Performance for Functional Molecule, College of Chemistry, Tianjin Normal University, Tianjin 300387, PR China*

Yi Yun Zhang − *Key Laboratory of Inorganic-Organic Hybrid Functional Material Chemistry (Tianjin Normal University), Ministry of Education, Tianjin Key Laboratory of Structure and Performance for Functional Molecule, College of Chemistry, Tianjin Normal University, Tianjin 300387, PR China*

Na Jia Zhu − *Key Laboratory of Inorganic-Organic Hybrid Functional Material Chemistry (Tianjin Normal University), Ministry of Education, Tianjin Key Laboratory of Structure and Performance for Functional Molecule, College of Chemistry, Tianjin Normal University, Tianjin 300387, PR China*

Kuo Wang − *Key Laboratory of Inorganic-Organic Hybrid Functional Material Chemistry (Tianjin Normal University), Ministry of Education, Tianjin Key Laboratory of Structure and Performance for Functional Molecule, College of Chemistry, Tianjin Normal University, Tianjin 300387, PR China*

Ping Ping Sun − *Key Laboratory of Inorganic-Organic Hybrid Functional Material Chemistry (Tianjin Normal University),*

https://dx.doi.org/10.1021/acs.inorgchem.9b03272
Inorg. Chem. XXXX, XXX, XXX−XXX

Ministry of Education, Tianjin Key Laboratory of Structure and Performance for Functional Molecule, College of Chemistry, Tianjin Normal University, Tianjin 300387, PR China

Jian Zhong Huo − *Key Laboratory of Inorganic-Organic Hybrid Functional Material Chemistry (Tianjin Normal University), Ministry of Education, Tianjin Key Laboratory of Structure and Performance for Functional Molecule, College of Chemistry, Tianjin Normal University, Tianjin 300387, PR China; Key Laboratory of Advanced Energy Materials Chemistry (Ministry of Education), Collaborative Innovation Center of Chemical Science and Engineering (Tianjin), College of Chemistry, Nankai University, Tianjin 300071, PR China*

Complete contact information is available at: https://pubs.acs.org/10.1021/acs.inorgchem.9b03272

Notes

The authors declare no competing financial interest.

■ ACKNOWLEDGMENTS

This work was financially supported by Natural Science Foundation of Tianjin (Grant No. 18JCYBJC89700), Young Scientist Fund (Grant No. 21301128), the Science &Technology Development Fund of Tianjin Education Commission for Higher Education (2019ZD15), and the Program for Innovative Research Team in University of Tianjin (TD12-5038).

■ REFERENCES

(1) Loukopoulos, E.; Kostakis, G. E. Recent advances in the coordination chemistry of benzotriazole-based ligands. *Coord. Chem. Rev.* **2019**, *395*, 193−229.

(2) Song, T. Q.; Yuan, K.; Qiao, W. Z.; Shi, Y.; Dong, J.; Gao, H. L.; Yang, X. P.; Cui, J. Z.; Zhao, B. Water Stable [Tb_4] Cluster-Based Metal-Organic Framework as Sensitive and Recyclable Luminescence Sensor of Quercetin. *Anal. Chem.* **2019**, *91*, 2595−2599.

(3) Zou, J. Y.; Li, L.; You, S. Y.; Chen, K. H.; Dong, X. Na.; Chen, Y. H.; Cui, J. Z. A usf Zinc(II) Metal-Organic Framework as a Highly Selective Luminescence Probe for Acetylacetone Detection and Its Postsynthetic Cation Exchange. *Cryst. Growth Des.* **2018**, *18*, 3997−4003.

(4) Chen, H. M.; Wang, W. M.; Li, X. Q.; Chu, X. Y.; Nie, Y. Y.; Liu, Z.; Huang, S. X.; Shen, H. Y.; Cui, J. Z.; Gao, H. L. Luminescence and magnetocaloric effect of Ln_4 clusters (Ln = Eu, Gd, Tb, Er) bridged by CO_3^{2-} deriving from the spontaneous fixation of carbon dioxide in the atmosphere. *Inorg. Chem. Front.* **2018**, *5*, 394−402.

(5) Zhao, J.; Liu, X.; Wu, Y. P.; Li, D. S.; Zhang, Q. C. Surfactants as promising media in the field of metal-organic frameworks. *Coord. Chem. Rev.* **2019**, *391*, 30−43.

(6) Xiao, J. N.; Liu, J. J.; Liu, M. Y.; Ji, G. F.; Liu, Z. L. Fabrication of a Luminescence-Silent System Based on a Post-Synthetic Modification Cd-MOFs: A Highly Selective and Sensitive Turn-on Luminescent Probe for Ascorbic Acid Detection. *Inorg. Chem.* **2019**, *58*, 6167−6174.

(7) Ji, G. F.; Gao, X. C.; Zheng, T. X.; Guan, W. H.; Liu, H. T.; Liu, Z. L. Postsynthetic Metalation Metal-Organic Framework as a Fluorescent Probe for the Ultrasensitive and Reversible Detection of PO_4^{3-} Ions. *Inorg. Chem.* **2018**, *57*, 10525−10532.

(8) Ji, G. F.; Zheng, T. X.; Gao, X. C.; Liu, Z. L. A highly selective turn-on luminescent logic gates probe based on post-synthetic MOF for aspartic acid detection. *Sens. Actuators, B* **2019**, *284*, 91−95.

(9) Song, X. Z.; Song, S. Y.; Zhao, S. N.; Hao, Z. M.; Zhu, M.; Meng, X.; Wu, L. L.; Zhang, H. J. Single-Crystal-to-Single-Crystal Transformation of a Europium(III) Metal-Organic Framework Producing a Multi-responsive Luminescent Sensor. *Adv. Funct. Mater.* **2014**, *24*, 4034−4041.

(10) Zhao, S. N.; Li, L. J.; Song, X. Z.; Zhu, M.; Hao, Z. M.; Meng, X.; Wu, L. L.; Feng, J.; Song, S. Y.; Wang, C.; Zhang, H. J. Lanthanide Ion Codoped Emitters for Tailoring Emission Trajectory and Temperature Sensing. *Adv. Funct. Mater.* **2015**, *25*, 1463−1469.

(11) Wu, L. L.; Wang, Z.; Zhao, S. N.; Meng, X.; Song, X. Z.; Feng, J.; Song, S. Y.; Zhang, H. J. A Metal-Organic Framework/DNA Hybrid System as a Novel Fluorescent Biosensor for Mercury(II) Ion Detection. *Chem. - Eur. J.* **2016**, *22*, 477−480.

(12) Li, S. Q.; Hu, X.; Chen, Q. M.; Zhang, X. D.; Chai, H. X.; Huang, Y. M. Introducing bifunctional metal-organic frameworks to the construction of a novel ratiometric fluorescence sensor for screening acid phosphatase activity. *Biosens. Bioelectron.* **2019**, *137*, 133−139.

(13) Liu, C.; Yan, B. A novel photofunctional hybrid material of pyrene functionalized metal-organic framework with conformation change for fluorescence sensing of Cu^{2+}. *Sens. Actuators, B* **2016**, *235*, 541−546.

(14) Hao, J.; Yan, B. Highly sensitive and selective fluorescent probe for Ag^+ based on a Eu^{3+} post-functionalized metal-organic framework in aqueous media. *J. Mater. Chem. A* **2014**, *2*, 18018−18025.

(15) Hao, J.; Yan, B. Ag^+-sensitized lanthanide luminescence in Ln^{3+} post-functionalized metal-organic frameworks and Ag^+ sensing. *J. Mater. Chem. A* **2015**, *3*, 4788−4792.

(16) Rybak, J. C.; Tegel, M.; Johrendt, D.; Muller-Buschbaum, K. Polymorphism of isotypic series of homoleptic 1,2,3-triazolate MOFs [Ln(Tz*)3] containing the heavy lanthanides Gd-Lu: from open to dense frameworks of varying dimensionality. *Z. Kristallogr. - Cryst. Mater.* **2010**, *225*, 187−194.

(17) Zhang, S. Y.; Shi, W.; Cheng, P.; Zaworotko, M. J. A Mixed-Crystal Lanthanide Zeolite-like Metal-Organic Framework as a Fluorescent Indicator for Lysophosphatidic Acid, a Cancer Biomarker. *J. Am. Chem. Soc.* **2015**, *137*, 12203−12206.

(18) Zhou, J. M.; Li, H. H.; Zhang, H.; Li, H. M.; Shi, W.; Cheng, P. A Bimetallic Lanthanide Metal-Organic Material as a Self-Calibrating Color-Gradient Luminescent Sensor. *Adv. Mater.* **2015**, *27*, 7072−7077.

(19) Wu, S. Y.; Lin, Y. N.; Liu, J. W.; Shi, W.; Yang, G. M.; Cheng, P. Rapid Detection of the Biomarkers for Carcinoid Tumors by a Water Stable Luminescent Lanthanide Metal-Organic Framework Sensor. *Adv. Funct. Mater.* **2018**, *28*, 1707169.

(20) Jin, M.; Mou, Z. L.; Zhang, R. L.; Liang, S. S.; Zhang, Z. Q. An efficient ratiometric fluorescence sensor based on metal-organic frameworks and quantum dots for highly selective detection of 6-mercaptopurine. *Biosens. Bioelectron.* **2017**, *91*, 162−168.

(21) Zhao, D.; Yue, D.; Zhang, L.; Jiang, K.; Qian, G. D. Cryogenic Luminescent Tb/Eu-MOF Thermometer Based on a Fluorine-Modified Tetracarboxylate Ligand. *Inorg. Chem.* **2018**, *57*, 12596−12602.

(22) Zhao, S. Q.; Chen, D.; Wei, F. H.; Chen, N. N.; Liang, Z.; Luo, Y. Removal of Congo red dye from aqueous solution with nickel-based metal-organic framework/graphene oxide composites prepared by ultrasonic wave-assisted ball milling. *Ultrason. Sonochem.* **2017**, *39*, 845−852.

(23) Israr, F.; Kim, D. K.; Kim, Y.; Oh, S. J.; Ng, K. C.; Chun, W. Synthesis of porous Cu-BTC with ultrasonic treatment: Effects of ultrasonic power and solvent condition. *Ultrason. Sonochem.* **2016**, *29*, 186−193.

(24) Hakimifar, A.; Morsali, A. High-sensitivity detection of nitroaromatic compounds (NACs) by the pillared-layer metal-organic framework synthesized via ultrasonic method. *Ultrason. Sonochem.* **2019**, *52*, 62−68.

(25) Adem, S.; Ciftci, M. Effects of some drugs on human erythrocyte 6-phosphogluconate dehydrogenase: an in vitro study. *J. Enzyme Inhib. Med. Chem.* **2007**, *22*, 751−754.

(26) Bakshi, M.; Singh, B.; Singh, A.; Singh, S. The ICH guidance in practice: stress degradation studies on ornidazole and development of a validated stability-indicating assay. *J. Pharm. Biomed. Anal.* **2001**, *26*, 891−897.

(27) Baltaci, D.; Akyazi, H.; Kandis, H.; Saritas, A.; Mungan, S.; Kara, I. H. Ornidazole-induced fixed drug eruption: A case report. *Zdr. Vestn.* **2012**, *81*, 337−340.
(28) Boison, J. O.; Asea, P. A.; Matus, J. L. Validation of a new screening, determinative, and confirmatory multi-residue method for nitroimidazoles and their hydroxy metabolites in turkey muscle tissue by liquid chromatography-tandem mass spectrometry. *Drug Test. Anal.* **2012**, *4*, 130−138.
(29) Bader, C.; Chelladurai, J. J.; Thompson, K.; Hall, C.; Carlson, S. A.; Brewer, M. T. Evaluation of high-throughput assays for in vitro drug susceptibility testing of Tritrichomonas foetus trophozoites. *Vet. Parasitol.* **2016**, *223*, 34−37.
(30) Bissett, S. A.; Gowan, R. A.; O'Brien, C. R.; Stone, M. R.; Gookin, J. L. Feline diarrhoea associated with Tritrichomonas cf. foetus and Giardia co-infection in an Australian cattery. *Aust. Vet. J.* **2008**, *86*, 440−443.
(31) Liu, X. Y.; Liu, B.; Li, G. H.; Liu, Y. L. Two anthracene-based metal-organic frameworks for highly effective photodegradation and luminescent detection in water. *J. Mater. Chem. A* **2018**, *6*, 17177−17185.
(32) Zhai, Z. W.; Yang, S. H.; Cao, M.; Li, L. K.; Du, C. X.; Zang, S. Q. Rational Design of Three Two-Fold Interpenetrated Metal-Organic Frameworks: Luminescent Zn/Cd-Metal-Organic Frameworks for Detection of 2,4,6-Trinitrophenol and Nitrofurazone in the Aqueous Phase. *Cryst. Growth Des.* **2018**, *18*, 7173−7182.
(33) Blessmann, J.; Le Van, A.; Tannich, E. Hepatic ultrasound in a population with high incidence of invasive amoebiasis: evidence for subclinical, self-limited amoebic liver abscesses. *Trop. Med. Int. Health* **2003**, *8*, 231−233.
(34) Bruchhaus, I.; Roeder, T.; Lotter, H.; Schwerdtfeger, M.; Tannich, E. Differential gene expression in Entamoeba histolytica isolated from amoebic liver abscess. *Mol. Microbiol.* **2002**, *44*, 1063−1072.
(35) Cruz-Baquero, A.; Jaramillo, L. M. C.; Gutierrez-Meza, M.; Jarillo-Luna, R. A.; Campos-Rodriguez, R.; Rivera-Aguilar, V.; Miliar-Garcia, A.; Pacheco-Yepez, J. Different behavior of myeloperoxidase in two rodent amoebic liver abscess models. *PLoS One* **2017**, *12*, e0182480.
(36) Ramos-Martinez, E.; Olivos-Garcia, A.; Saavedra, E.; Nequiz, M.; Sanchez, E. C.; Tello, E.; El-Hafidi, M.; Saralegui, A.; Pineda, E.; Delgado, J.; Montfort, I.; Perez-Tamayo, R. Entamoeba histolytica: Oxygen resistance and virulence. *Int. J. Parasitol.* **2009**, *39*, 693−702.
(37) Xiao, J. N.; Liu, J. J.; Liu, M. Y.; Ji, G. F.; Liu, Z. L. Fabrication of a Luminescence-Silent System Based on a Post-Synthetic Modification Cd-MOFs: A Highly Selective and Sensitive Turn-on Luminescent Probe for Ascorbic Acid Detection. *Inorg. Chem.* **2019**, *58*, 6167−6174.
(38) Wang, X. R.; Huang, Z.; Du, J.; Wang, X. Z.; Gu, N.; Tian, X.; Li, Y.; Liu, Y. Y.; Huo, J. Z.; Ding, B. Hydrothermal Preparation of Five Rare-Earth (Re = Dy, Gd, Ho, Pr, and Sm) Luminescent Cluster-Based Coordination Materials: The First MOFs-based Ratiometric Fluorescent Sensor for Lysine and Bifunctional Sensing Platform for Insulin and Al^{3+}. *Inorg. Chem.* **2018**, *57*, 12885−12899.
(39) Wang, X. R.; Wang, X. Z.; Li, Y.; Liu, K.; Liu, S. X.; Du, J.; Huang, Z.; Luo, Y.; Huo, J. Z.; Wu, X. X.; Liu, Y. Y.; Ding, B. Sonochemical synthesis of a multi-responsive regenerable water-stable zinc (II) fluorescent probe for highly selective, sensitive and real-time sensing of benzaldehyde, ferric ion and PH. *Ultrason. Sonochem.* **2018**, *44*, 340−349.
(40) Han, J. Q.; Lu, K. Y.; Yue, Y. Y.; Mei, C. T.; Wang, H. X.; Yan, P. B.; Xu, X. W. Synthesis And electrochemical performance of flexible cellulose nanofiber-carbon nanotube/natural rubber composite elastomers as supercapacitor electrodes. *New Carbon Mater.* **2018**, *33*, 341−350.
(41) Jiang, S. H.; Han, D. H.; Huang, C. B.; Duan, G. G.; Hou, H. Q. Temperature-induced molecular orientation and mechanical properties of single electrospun polyimide nanofiber. *Mater. Lett.* **2018**, *216*, 81−83.
(42) Zhou, S. Z.; Zhou, G. Y.; Jiang, S. H.; Fan, P. C.; Hou, H. Q. Flexible and refractory tantalum carbide-carbon electrospun nanofibers with high modulus and electric conductivity. *Mater. Lett.* **2017**, *200*, 97−100.
(43) Lv, D.; Wang, R.; Tang, G.; Mou, Z.; Lei, J.; Han, J.; De Smedt, S.; Xiong, R.; Huang, C. Ecofriendly Electrospun Membranes Loaded with Visible-Light- Responding Nanoparticles for Multifunctional Usages: Highly Efficient Air Filtration, Dye Scavenging, and Bactericidal Activity. *ACS Appl. Mater. Interfaces* **2019**, *11*, 12880−12889.
(44) Ju, J. J.; Peng, X. F.; Huang, K. Q.; Li, L. W.; Liu, X. H.; Chitrakar, C.; Chang, L. Q.; Gu, Z. P.; Kuang, T. R. High-performance porous PLLA-based scaffolds for bone tissue engineering: Preparation, characterization, and in vitro and in vivo evaluation. *Polymer* **2019**, *180*, 121707.
(45) Zhou, Z. P.; Chen, F. C.; Wu, L.; Kuang, T. R.; Liu, X. H.; Yang, J. T.; Fan, P.; Fei, Z. D.; Zhao, Z. P.; Zhong, M. Q. Heteroatoms-doped 3D carbon nanosphere cages embedded with MoS2 for lithium-ion battery. *Electrochim. Acta* **2020**, *332*, 135490.
(46) Zhang, Y. H.; Li, B.; Ma, H. P.; Zhang, L. M.; Zheng, Y. X. Rapid and facile ratiometric detection of an anthrax biomarker by regulating energy transfer process in bio-metal-organic framework. *Biosens. Bioelectron.* **2016**, *85*, 287−293.
(47) Dong, M. J.; Zhao, M.; Ou, S.; Zou, C.; Wu, C. D. A Luminescent Dye@MOF Platform: Emission Fingerprint Relationships of Volatile Organic Molecules. *Angew. Chem., Int. Ed.* **2014**, *53*, 1575−1579.
(48) Qu, X.; Yan, B. Stable Tb(III)-Based Metal-Organic Framework: Structure, Photoluminescence, and Chemical Sensing of 2-Thiazolidinethione-4-carboxylic Acid as a Biomarker of CS_2. *Inorg. Chem.* **2019**, *58*, 524−534.
(49) Dong, B. X.; Pan, Y. M.; Liu, W. L.; Teng, Y. L. An Ultrastable Luminescent Metal-Organic Framework for Selective Sensing of Nitroaromatic Compounds and Nitroimidazole-Based Drug Molecules. *Cryst. Growth Des.* **2018**, *18*, 431−440.
(50) Zhao, Y.; Wang, Y. J.; Wang, N.; Zheng, P.; Fu, H. R.; Han, M. L.; Ma, L. F.; Wang, L. Y. Tetraphenylethylene-Decorated Metal-Organic Frameworks as Energy-Transfer Platform for the Detection of Nitro-Antibiotics and White-Light Emission. *Inorg. Chem.* **2019**, *58*, 12700−12706.
(51) Zhang, Q. F.; Lei, M. Y.; Yan, H.; Wang, J. Y.; Shi, Y. A Water-Stable 3D Luminescent Metal-Organic Framework Based on Heterometallic $[Eu^{III}_6Zn^{II}]$ Clusters Showing Highly Sensitive, Selective, and Reversible Detection of Ronidazole. *Inorg. Chem.* **2017**, *56*, 7610−7614.
(52) Fu, H. R.; Zhao, Y.; Xie, T.; Han, M. L.; Ma, L. F.; Zang, S. Q. Stable dye-encapsulated indium-organic framework as dual-emitting sensor for the detection of Hg^{2+}/$Cr_2O_7^{2-}$ and a wide range of nitro-compounds. *J. Mater. Chem. C* **2018**, *6*, 6440−6448.
(53) Fu, H. R.; Yan, L. B.; Wu, N. T.; Ma, L. F.; Zang, S. Q. Dual-emission MOF⊃dye sensor for ratiometric fluorescence recognition of RDX and detection of a broad class of nitro-compounds. *J. Mater. Chem. A* **2018**, *6*, 9183−9191.
(54) Wang, H. S.; Liu, H. L.; Wang, K.; Ding, Y.; Xu, J. J.; Xia, X. H.; Chen, H. Y. Insight into the Unique Fluorescence Quenching Property of Metal-Organic Frameworks upon DNA Binding. *Anal. Chem.* **2017**, *89*, 11366−11371.

https://dx.doi.org/10.1021/acs.inorgchem.9b03272
Inorg. Chem. XXXX, XXX, XXX−XXX